

## Supporting information

### Interfacial Chemistry Modulation via Amphoteric Glycine for Highly Reversible Zinc Anode

Yu Liu,<sup>#, a, b</sup> Yongkang An,<sup>#, a</sup> Lu Wu,<sup>a</sup> Jianguo Sun,<sup>b</sup> Fangyu Xiong,<sup>a</sup> Han Tang,<sup>a</sup> Shulin Chen,<sup>a</sup> Yue Guo,<sup>b</sup> Lei Zhang,<sup>a</sup> Qinyou An,<sup>\*, a, c</sup> Liqiang Mai<sup>\*, a, c</sup>

<sup>a</sup>State Key Laboratory of Advanced Technology for Materials Synthesis and Processing, Wuhan University of Technology, Wuhan 430070, China

<sup>b</sup>Department of Materials Science and Engineering, National University of Singapore, Singapore, 117574 Singapore

<sup>c</sup>Foshan Xianhu Laboratory of the Advanced Energy Science and Technology Guangdong Laboratory, Xianhu Hydrogen Valley, Foshan 528200, China

\* Corresponding Author: Prof. Liqiang Mai, e-mail: mlq518@whut.edu.cn; Prof. Qinyou An, e-mail: anqinyou86@whut.edu.cn

## Experimental section

**Materials Characterization:** The crystal structures are evaluated by a Bruker D8 Advance X-ray diffractometer with Cu K $\alpha$  radiation. Fourier-transform infrared spectra were recorded on a Nicolet Nexus 670 Fourier transform infrared spectrometer (FT-IR). Nuclear magnetic resonance (NMR) spectra were obtained on a Bruker Avance II 300MHz NMR spectrometer. Raman spectra were collected using a confocal Raman microscope (LabRAM HR800). The morphologies of samples are conducted using field emission scanning electron microscopy (FESEM; JEOL JSM-7100F, 20 kV). TEM, HR-TEM, and EDS mapping were performed on a JEM-2100F transmission electron microscope. at 200 kV. The chemical state and composition were evaluated by an X-ray photoelectron spectroscopy (XPS, AXIS SUPRA+).

**Electrochemical Characterization:** For symmetric batteries, asymmetric batteries, and full cells assembled in CR2025 type cell, the Zn plates as counter and reference electrode, the Whatman glass fiber membrane was chosen as the separator, the electrolyte was ZnSO<sub>4</sub> or Gly/ZnSO<sub>4</sub> electrolytes, Zn plate, Cu plate, NH<sub>4</sub>V<sub>4</sub>O<sub>10</sub> as work electrodes, respectively. Zn metal and Cu metal were polished before use. Tafel plots, chronoamperometry curves and hydrogen evolution curves were measured in ZnSO<sub>4</sub> and Gly/ZnSO<sub>4</sub> electrolyte using a three-electrode system with Zn foil as the working electrode, Pt plate as the counter electrode, and Ag/AgCl as the reference electrode, respectively. The CV curves of NaSO<sub>4</sub> and Gly/Na<sub>2</sub>SO<sub>4</sub> electrolyte were

measured using a three-electrode system with Ti foil as the working electrode, Pt plate as the counter electrode, and Ag/AgCl as the reference electrode, respectively.

### **MD Simulations and DFT calculations method**

*Molecular dynamics (MD) simulations:* Classical MD simulations were performed using the gromacs 2019.5 software package.<sup>1,2</sup> All the parameters of the ion are adopt GAFF2 force field.<sup>3</sup> The other molecules were optimized via gaussian 16 package at a level of B3LYP/def2tzvp firstly, and vibration analysis was performed at the same level to ensure that there are no virtual frequencies. The ACPYPE webserver ( <https://www.bio2byte.be/acpype/> ) was employed to obtain their GAFF2 force field topology file.<sup>4</sup> The initial structure of the simulation system adopts the Packing Optimization for Molecular Dynamics Simulations (Packmol) program.<sup>5</sup> The size of box is  $5 \times 5 \times 5 \text{ nm}^3$ , and periodic boundary conditions were set in all three directions. The simulation cells contained 1100 H<sub>2</sub>O, 40 ZnSO<sub>4</sub>, and 10 Gly. The simulation process was detailed as follows:

the 5000-step steepest descent method and 5000-step conjugate gradient method were used to avoid unreasonable contact of the system. NPT ensemble was used to pre-equilibrate the system, and V-rescale temperature coupling and parrinello-rahman pressure coupling were used to control the temperature to 298 K, the pressure was maintained at 1 atm, the non-bonding cutoff radius was 1.2 nm, and the integration step was 2 fs.

Finally, 30 ns simulation was performed, and the bond length and angle were constrained by the LINCS algorithm. The two-way intercept was set to 1.2 nm, van der Waals interaction, and the long-distance electrostatic interaction was set by the particle-mesh Ewald method. The trajectory file during simulation was saved every 10.0 ps.

***Electrostatic potential (ESP) calculations:*** The ESP calculations were conducted using the GaussView package in Gaussian (G09) program. The structure optimization was performed at M062x/6-311+g(d) level.

***DFT calculations:*** All calculations in our work were performed under the Vienna Ab initio Simulation Package (VASP) code.<sup>6</sup> The projector augmented wave (PAW) method was used to calculate the ion-electron interaction.<sup>7, 8</sup> The electronic exchange and correlation were approximated by the Perdew-Burke- Ernzerhof (PBE) with the kinetic cutoff energy of 520 eV.<sup>9</sup> Most importantly, considering the weak interactions cannot be described accurately using the standard PBE functional, empirical atom-pairwise corrections proposed by DFT-D3 scheme with Becke-Jonson damping was applied to describe the long-range van der Waals interactions.<sup>10, 11</sup> The Brillouin zone was sampled using the Monkhorst-Pack scheme with the sizes of  $3 \times 3 \times 1$  k-meshes for the structural relaxation and adsorption energy calculation in Zn slab system.<sup>12</sup> A 20 Å vacuum along the z-direction was utilized to prevent spurious interaction between the periodically repeated images. For geometry optimization, all atoms were fully relaxed until the energies and residual forces on each atom converged to  $10E-5$  eV and 0.02 eV Å<sup>-1</sup>, respectively. In addition, the Zn (002) slab is constructed with lattice constants of

$a = 10.5011 \text{ \AA}$ ,  $b = 9.0943$ ,  $c = 31.9695 \text{ \AA}$  and  $\alpha = \beta = \gamma = 90^\circ$ . And the adsorbate (one Glycine or  $\text{H}_2\text{O}$  molecular) is put on the clean surface of Zn (002) slab. two different initial states of the glycine adsorbed on Zn surface are set to search for the most stable adsorption structure.

The adsorption energy ( $E_{ads}$ ) of each adsorbate on Zn clean surface was calculated according to

$$E_{ads} = E_{total} - E_{Zn} - E_{sub}$$

where  $E_{Zn}$ ,  $E_{sub}$  and  $E_{total}$  are the energy of, respectively, Zn clean surface system, only adsorbate system and the system of adsorbate anchored on Zn surface.

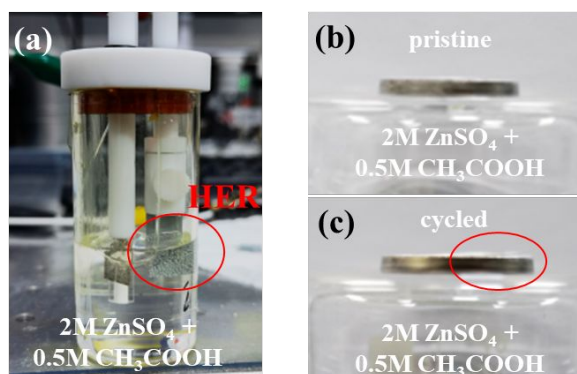


**Figure S1.** (a) The Zn soaked in 2M ZnSO<sub>4</sub>+0.5M CH<sub>3</sub>COOH electrolyte at rest. The Zn Symmetrical battery with 2M ZnSO<sub>4</sub>+0.5M CH<sub>3</sub>COOH; (b) pristine, (c) after cycled.

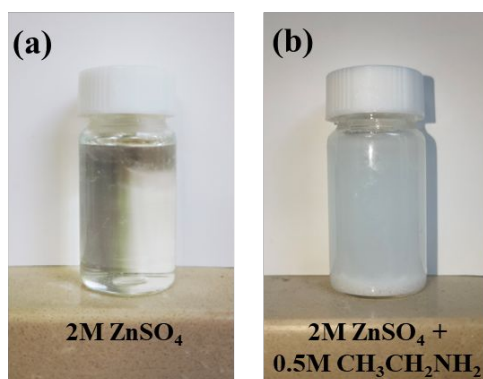


**Figure S2.** (a) 2M ZnSO<sub>4</sub>, (b) 2M ZnSO<sub>4</sub>+0.5M CH<sub>3</sub>CH<sub>2</sub>NH<sub>2</sub>.

Glycine molecules are ionizable in water and can be considered derivatives of acetic acid or aminoethane. However, compared with acetic acid or aminoethane, glycine is more suitable as an additive because the acetic acid additive will reduce the electrolyte pH and accelerate HER (Figure S1), and the aminoethane additive will cause the zinc ions precipitation (Figure S2) that will result in the opposite effect.

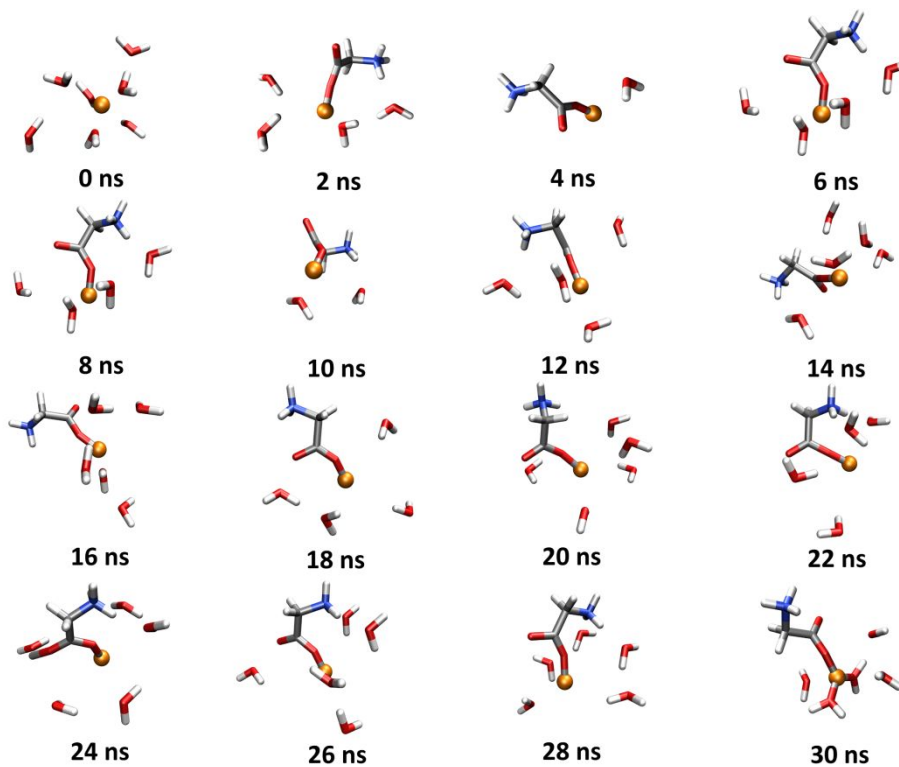


Figure S3. The evolution process of  $\text{Zn}^{2+}$  solvation shell structure.

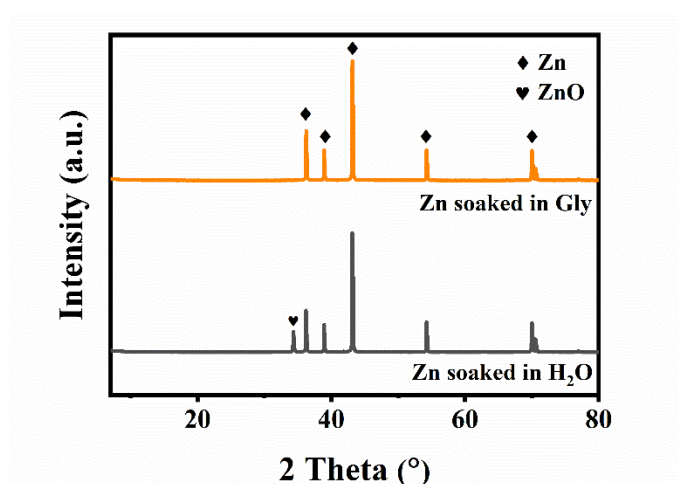


Figure S4. XRD spectra of Zn anode soaked in  $\text{H}_2\text{O}$  and Gly electrolyte for 5 days.

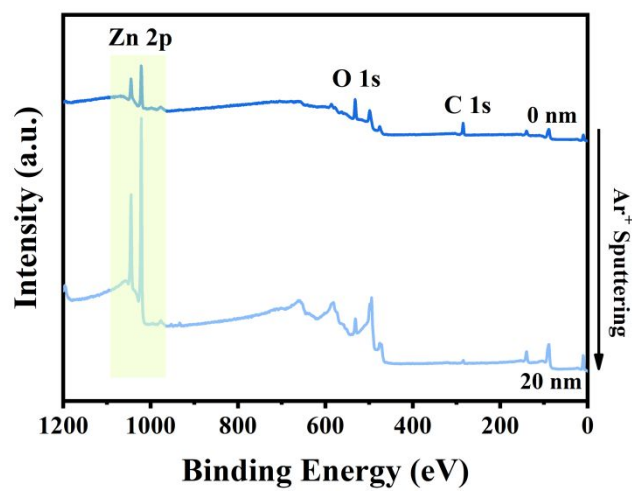


Figure S5. XPS spectra of Zn soaked in Gly and that after sputtering

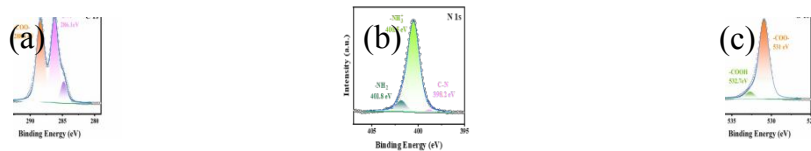
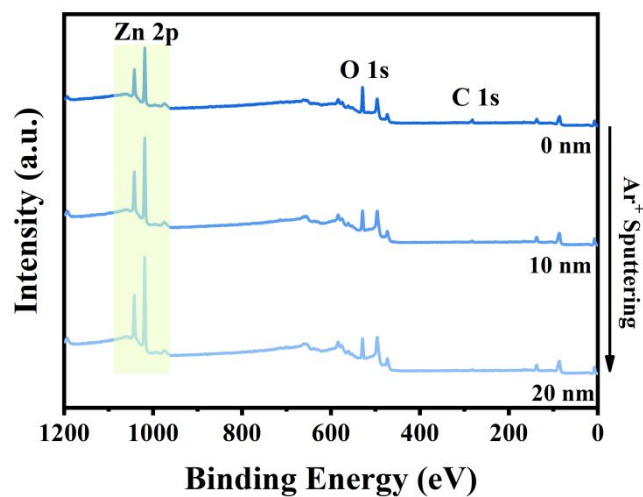
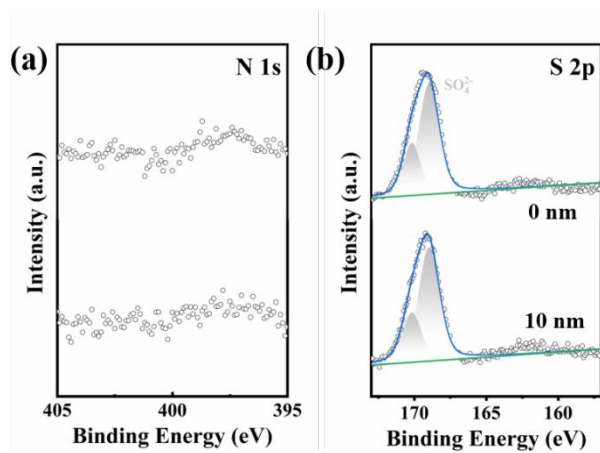


Figure S6. High-resolution C 1s, N 1s, O 1s XPS spectra of Gly.



**Figure S7.** XPS depth profile of Zn anode surface using in Gly/ZnSO<sub>4</sub> electrolyte for 20 cycles.



**Figure S8.** XPS depth profile for N 1s, and S 2p of Zn anode surface using in bare ZnSO<sub>4</sub> electrolyte for 20 cycles.

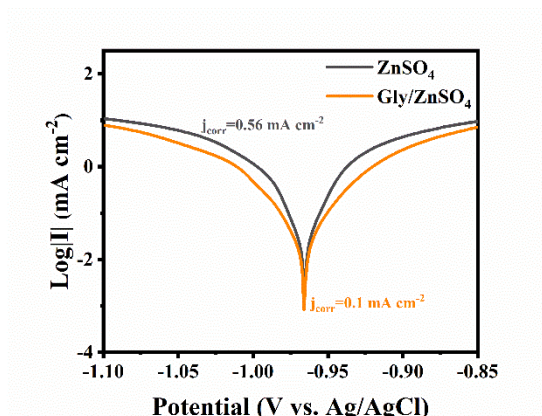


**Figure S9.** Tafel plots of Zn plate tested in  $\text{ZnSO}_4$  and  $\text{Gly/ZnSO}_4$  electrolyte at a scan rate of  $1 \text{ mV s}^{-1}$  using a three-electrode system.

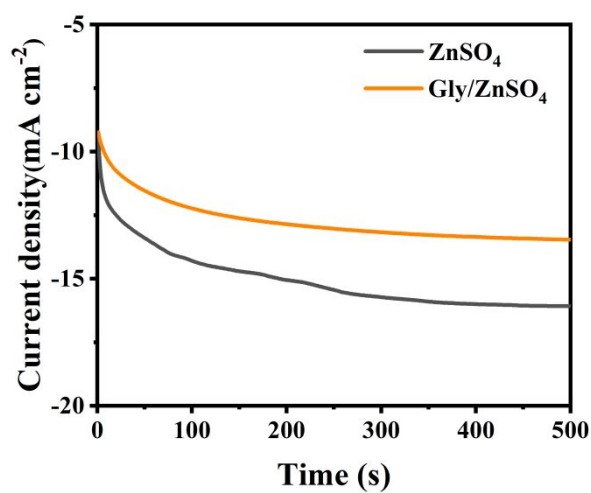


**Figure S10.** Chronoamperometry curves of the Zn tested in  $\text{ZnSO}_4$  and  $\text{Gly/ZnSO}_4$  electrolyte at the constant potential of -150 mV.

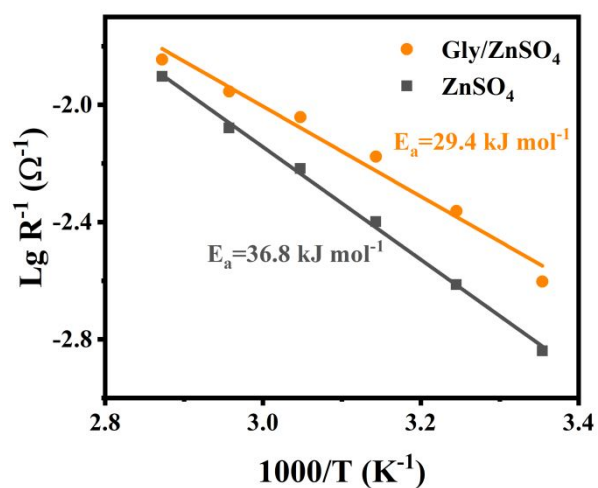


**Figure S11.** Comparison of Arrhenius curves and activation energies of Zn//Zn symmetric cells using ZnSO<sub>4</sub> and Gly/ZnSO<sub>4</sub> electrolyte after 20 cycles.

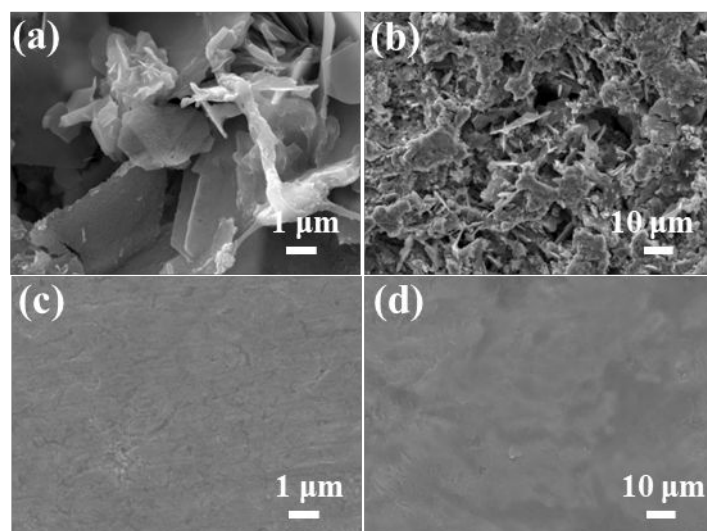


**Figure S12.** SEM image of the Zn deposited in (a-b) ZnSO<sub>4</sub> and (c-d) Gly/ZnSO<sub>4</sub> for 20 cycles.

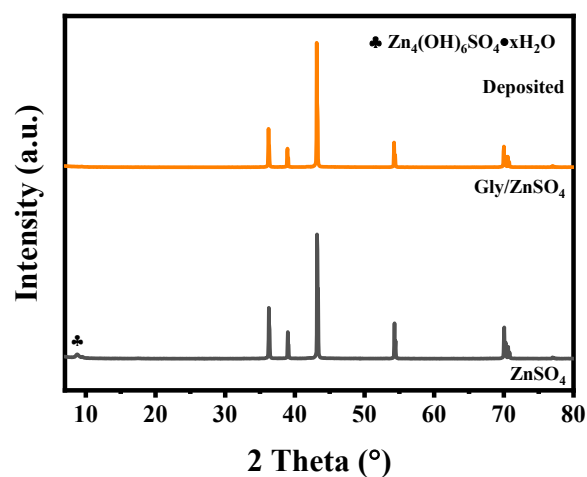


**Figure S13.** XRD spectra of Zn anode tested in  $\text{ZnSO}_4$  and  $\text{Gly/ZnSO}_4$  electrolyte for 20 cycles in a current density of  $1\text{ mA cm}^{-2}$  with an area capacity of  $1\text{ mAh cm}^{-2}$ .

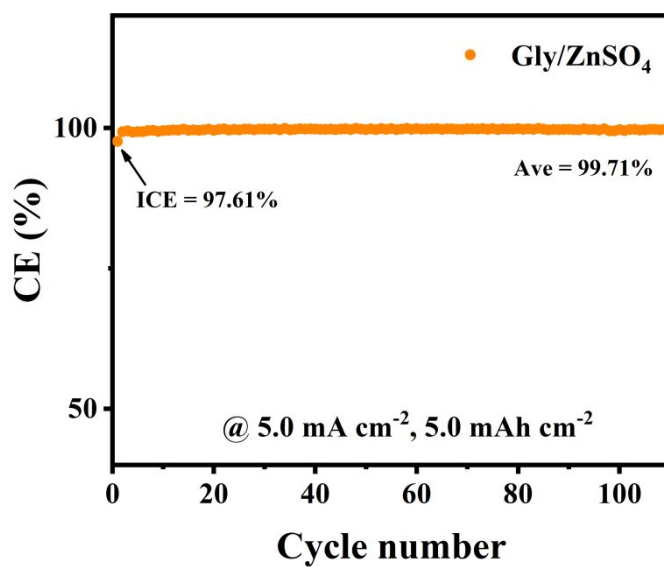


**Figure S14.** Coulombic efficiency of Zn//Cu batteries using  $\text{Gly/ZnSO}_4$  at  $5\text{ mA cm}^{-2}$  with a capacity of  $5\text{ mAh cm}^{-2}$ .

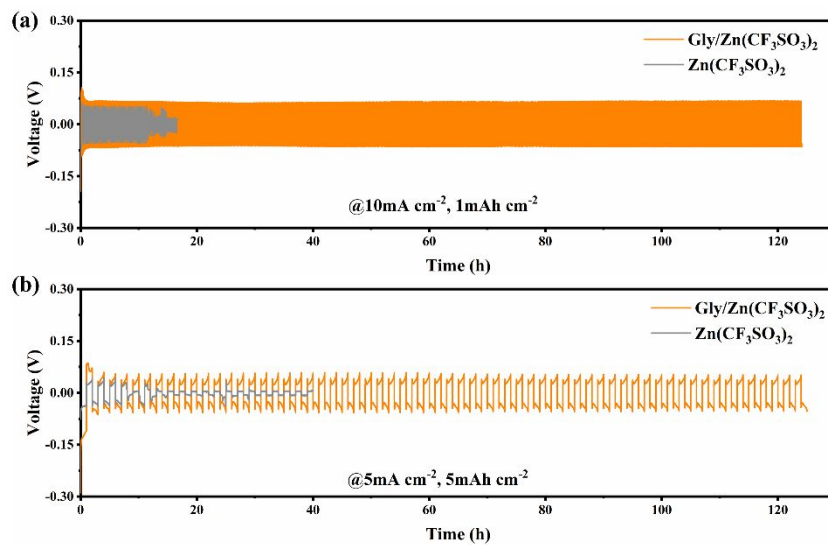


**Figure S15.** Cycling stability comparison of Zn//Zn symmetric cells using Zn(CF<sub>3</sub>SO<sub>3</sub>)<sub>2</sub> and Gly/Zn(CF<sub>3</sub>SO<sub>3</sub>)<sub>2</sub> electrolyte at (a) 10 mA cm<sup>-2</sup> / 1 mAh cm<sup>-2</sup> and (b) 5 mA cm<sup>-2</sup> / 5 mAh cm<sup>-2</sup>.

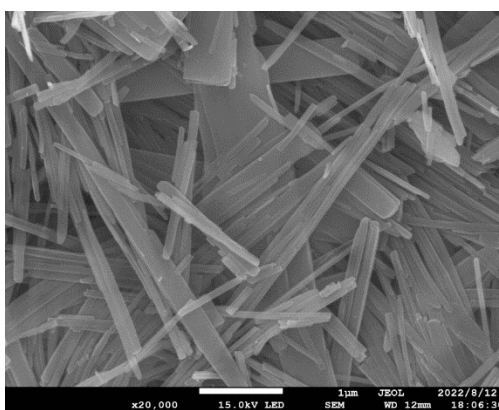


**Figure S16.** SEM image of NVO.

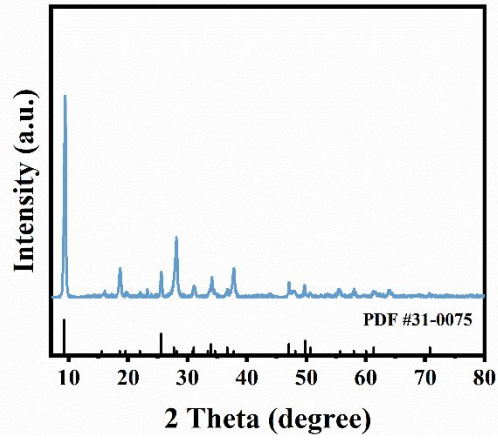


Figure S17. XRD pattern of NVO.

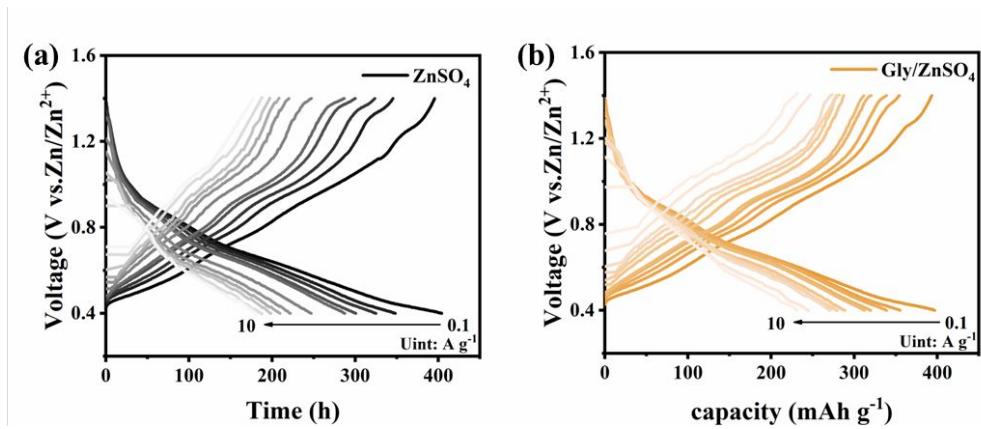


Figure S18. Voltage profiles of Zn//NVO full cells in (a)  $\text{ZnSO}_4$  and (b)  $\text{Gly/ZnSO}_4$  electrolytes at various current densities.

## References

- (1) Yang, H.; Chen, X.; Yao, N.; Piao, N.; Wang, Z.; He, K.; Cheng, H.-M.; Li, F., Dissolution–Precipitation Dynamics in Ester Electrolyte for High-Stability Lithium Metal Batteries. *ACS Energy Lett.* **2021**, *6*, 1413-1421.
- (2) Fu, J.; Ji, X.; Chen, J.; Chen, L.; Fan, X.; Mu, D.; Wang, C., Lithium Nitrate Regulated Sulfone Electrolytes for Lithium Metal Batteries. *Angew. Chem. Int. Ed.* **2020**, *59*, 22194-22201.
- (3) Wang, J.; Wolf, R. M.; Caldwell, J. W.; Kollman, P. A.; Case, D. A., Development and testing of a general amber force field. *J. Comput. Chem.* **2004**, *25*, 1157-1174.
- (4) Bernardi, A.; Faller, R.; Reith, D.; Kirschner, K. N., ACPYPE update for nonuniform 1–4 scale factors: Conversion of the GLYCAM06 force field from AMBER to GROMACS. *SoftwareX* **2019**, *10*, 100241.
- (5) Martinez, L.; Andrade, R.; Birgin, E. G.; Martinez, J. M., PACKMOL: a package for building initial configurations for molecular dynamics simulations. *J. Comput. Chem.* **2009**, *30*, 2157-2164.
- (6) Kresse, G.; Furthmuller, J., Efficient iterative schemes for ab initio total-energy calculations using a plane-wave basis set. *Phy. Rev. B* **1996**, *54*, 11169-11186.
- (7) Kresse, G.; Joubert, D., From ultrasoft pseudopotentials to the projector augmented-wave method. *Phy. Rev. B* **1999**, *59*, 1758-1775.
- (8) Blochl, P. E., Projector augmented-wave method. *Phy. Rev. B* **1994**, *50*, 17953-17979.

- (9) Perdew, J. P.; Burke, K.; Ernzerhof, M., Generalized Gradient Approximation Made Simple. *Physical Review Letters* **1996**, *77*, 3865-3868.
- (10) Grimme, S.; Antony, J.; Ehrlich, S.; Krieg, H., A consistent and accurate ab initio parametrization of density functional dispersion correction (DFT-D) for the 94 elements H-Pu. *Journal of Chemical Physics* **2010**, *132*, 154104.
- (11) Grimme, S.; Ehrlich, S.; Goerigk, L., Effect of the damping function in dispersion corrected density functional theory. *J. Comput. Chem.* **2011**, *32*, 1456-1465.
- (12) Monkhorst, H. J.; Pack, J. D., Special points for Brillouin-zone integrations. *Phy. Rev. B* **1976**, *13*, 5188-5192.